ACCSCIENCE PUBLISHING

International Journal of Bioprinting

RESEARCH ARTICLE

Design and performance of 3D-printed cross-scale metamaterial porous structures for orthopedic implants

Guoqing Zhang[1]*, Junxin Li[2], Congcong Shangguan[3], Juanjuan Xie[1], Yongsheng Zhou[1], Aibing Huang[4], and Yuchao Bai[5]

[1]Department of Mechanical Design and Manufacturing, School of Mechanical and Electrical Engineering, Zhoukou Normal University, Zhoukou, Henan, China

[2]Contract Section, State owned Assets Management Office, Zhoukou Normal University, Zhoukou, Henan, China

[3]Veterinary Laboratory, Shangzhou District Animal Health Supervision Institute, Shangluo, Shaanxi, China

[4]Department of Orthopedics, Taizhou People's Hospital Affiliated to Nanjing Medical University, Taizhou, Jiangsu, China

[5]Department of Mechanical Engineering, School of Robotics and Advanced Manufacture, Harbin Institute of Technology, Shenzhen, Guangdong, China

(This article belongs to the *Special Issue*: *Additive Manufacturing of Functional Biomaterials-Series2*)

Abstract

The rising prevalence of orthopedic conditions in aging populations has created a growing demand for advanced implants with enhanced biocompatibility, mechanical performance, and tissue integration. To meet these demands, it is necessary to investigate the metamaterial properties of cross-scale porous structures, including both macroscale architecture and microscale texture. Accordingly, we employed parametric modeling to design porous structures; analyzed blood flow distribution through various multi-level porous designs using mold flow simulation; evaluated their compressive properties through finite element analysis; assessed biocompatibility via animal experiments; and obtained tissue ingrowth data using micro-computed tomography. The results indicated that when fluid flowed through cross-scale porous structures, the overall pressure was low, and the Kelvin cell structure exhibited favorable flow field characteristics under low pressure. When the structures were pressurized, texturization methods involving material removal resulted in larger displacements, while those involving material addition led to smaller displacements. The Kelvin cell structure exhibited extensive tissue ingrowth with a dense tissue pattern internally, and the amount of ingrowth decreased from the inside to the outside. Increasing the roughness of porous structures via material removal increased the surface-to-volume ratio to a certain extent but did not promote tissue ingrowth. In contrast, increasing roughness by material addition favored tissue ingrowth, laying a foundation for the design of cross-scale metamaterial implants.

Keywords: 3D printing; Biocompatibility; Mechanical properties; Metamaterial; Porous structure

***Corresponding author:**
Guoqing Zhang
(zhangguoqing1202@sohu.com)

Citation: Zhang G, Li J, Shangguan C, *et al*. Design and performance of 3D-printed cross-scale metamaterial porous structures for orthopedic implants. *Int J Bioprint*. 2025;11(6):515-530. doi: 10.36922/IJB025390401

Received: September 27, 2025
Revised: October 4, 2025
Accepted: October 11, 2025
Published online: October 14, 2025

1. Introduction

Aging is positively correlated with the incidence of orthopedic diseases. Currently, the population aged 60 and above in China has reached 264 million, with over 190 million aged 65 and above. Osteoporosis, fractures, osteoarthritis, dental cavities, and other bone diseases pose a significant threat to the health of the Chinese population.[1] In response to the growing demand for bone disease treatment, prosthetic replacement and repair of the affected area have emerged as effective solutions. Studies have shown that designing implants with personalized bio-fixed structures (partially or fully porous) can significantly improve biocompatibility, reduce weight, and minimize the risk of "stress shielding".[2,3] Novel multi-level porous structures have been widely applied in fields such as aeronautics, astronautics, and military technology due to their advantages, such as low relative density, high specific strength, high specific surface area, lightweight properties, sound and heat insulation, and good permeability. Therefore, studying the metamaterial properties of multi-level porous structures is crucial for the development of customized, integrated, lightweight, and cost-effective orthopedic implants with ultra-high mechanical and biomedical performance.

The advent of additive manufacturing (3D printing) technology has made it feasible to fabricate novel multi-level porous structures. 3D printing involves slicing a 3D model using specialized software to obtain sectional data, which is then input into a rapid prototyping device to manufacture solid parts by stacking the materials layer by layer. Owing to the layer-by-layer approach, 3D printing technology enables the production of components with virtually any geometric shape, offering advantages such as single-piece processing, small-batch production, complex geometries, and high-density finished parts.[4,5] Selective laser melting (SLM), a prominent 3D printing technology, is based on the laser melting of metal powders.[6]

Wang[7] evaluated the biocompatibility of titanium alloy samples produced by different 3D printing processes. *In vitro* cell experiments indicated no significant impact on the growth and osteogenic differentiation abilities of canine bone marrow mesenchymal stem cells (BMMSCs) in titanium alloy samples fabricated by both electron beam melting and SLM. Yang *et al.*[8] designed five titanium alloy scaffolds with different shapes and found that, during 3D printing, cell configuration and cell parameters significantly influenced the mechanical and permeability properties of triply periodic minimal surface unit cells. Wang[9] documented that artificial bone trabecular structures with uneven pore sizes were more conducive to the adhesion, proliferation, and differentiation of mouse pre-osteoblasts on titanium scaffolds than microporous structures with uniform pore sizes or dense solid structures, providing better osseointegration performance from a theoretical standpoint. Wang *et al.*[10] examined 3D printing-assisted internal fixation for complex tibial plateau fractures and found that it could shorten surgery duration, reduce intraoperative bleeding and fluoroscopy frequency, and improve patients' knee joint function, while effectively repositioning the articular surface. Zhang *et al.*[11] investigated the genotoxicity, hemolysis, *in vitro* cytotoxicity, post-implantation local reaction, intradermal reaction, skin sensitization, acute systemic toxicity, and subchronic toxicity of 3D-printed porous tantalum, with all experimental results meeting the requirements of GB/T 16886. Liang *et al.*[12] noted that porous structures can maintain cell morphology and facilitate the adhesion and proliferation of osteoblasts. This was not only conducive to the transport of nutrients and metabolites but also provided substantial physical space for the ingrowth of blood vessels and nerves, thereby enhancing the ingrowth and long-term stability of bone tissue. Liu *et al.*[13] demonstrated that the mechanical properties of 3D-printed porous Ti6Al4V titanium alloy scaffolds were influenced by their porous architecture, with initial strength well-suited to physiological demands. Furthermore, the materials exhibited excellent cellular biocompatibility. The 3D mesh structure in the porous scaffolds provided space for cell growth, enhanced the proliferative capacity of BMMSCs, and accelerated the growth of bone tissue into the micropores of titanium scaffolds. Lei *et al.*[14] used 3D printing technology to customize and manufacture structurally optimized porous pedicle screws, which enhanced bone regeneration and integration at the defect site, thereby improving the biological fixation of the implant *in vivo*. Tamaddon *et al.*[15] fabricated a porous titanium scaffold with 72% porosity using 3D printing technology and seeded sheep BMMSCs onto the surface for *in vitro* culture. The results indicated that the cells exhibited good adhesion on the scaffold surface. Zaharin *et al.*[16] examined the effects of cubic and helical micropores (300–600 μm in size) on the properties of porous titanium alloys. The results suggested that cubic structures were more suitable for implants, while all samples with helical structures remained viable candidates. Zadpoor[17] noted that alterations in the surface curvature of scaffolds can influence cell adhesion rates, cell migration, and morphology. Additionally, the growth rate of cells on concave surfaces was significantly higher than on convex and planar surfaces. Meanwhile, Kumar *et al.*[18] found that porous gradient scaffolds offered an ideal combination of porosity and mechanical properties for bone defect sites.

To date, extensive research has been conducted on the mechanical and biological properties of 3D-printed porous structures, which has partly improved the feasibility of their use in implants. However, significant potential remains for improving the metamaterial properties of these structures. Accordingly, the present study investigates the metamaterial properties and enhancement strategies for various cross-scale porous structures.

2. Materials and methods

2.1. Design methods

The design of metamaterial porous structures based on 3D printing should meet the following constraints[19–21]: (i) biocompatibility constraints – the pore size of porous scaffolds should range from 100 to 1000 μm, and the porosity should be between 50% and 90%. A higher surface-to-volume ratio is preferred. (ii) Manufacturing constraints: Sharp corners and thin walls should be larger than the diameter of the laser spot, and the minimum pore size should be greater than the diameter of the laser spot.

2.1.1. Design of different porous structures

Cylindrical porous scaffolds (n=3, ∅5×8 mm) were utilized for *in vivo* experiments. For ease of comparative analysis, the cylindrical porous structures were designed using the same parameters. The basic unit parameters of porous structures were as follows: unit radius = 0.7 mm, unit height = 1.3 mm, and strut diameter = 0.16 mm. The porous structures were designed using Rhinoceros (version 6.0, Robert McNeel & Associates, United States of America), a parametric modeling software, and the design results are shown in Figure 1. Table 1 lists the parameters of the designed porous structures. It can be observed from Table 1 that, under identical parameters, the Kelvin cell structure achieved a higher porosity.

2.1.2. Different texturization designs for the Kelvin cell structure

The surface morphology of porous structures can influence the biological functions of implants. Studies have shown that rougher surfaces with larger surface areas are favorable for cell adhesion.[22] For this reason, the Kelvin Cell porous structure, demonstrating relatively good overall performance, was selected for applying different forms of texturization in order to compare their effects on biological properties. Using secondary programming in Rhinoceros, four types of millimeter-scale surface textures were implemented on the Kelvin cell structure to explore how different surface morphologies affect biocompatibility. Cylindrical porous scaffolds (n=3, ∅5×8 mm) were used. For ease of comparative analysis, the structures were designed with identical parameters. The basic unit parameters were as follows: unit radius =

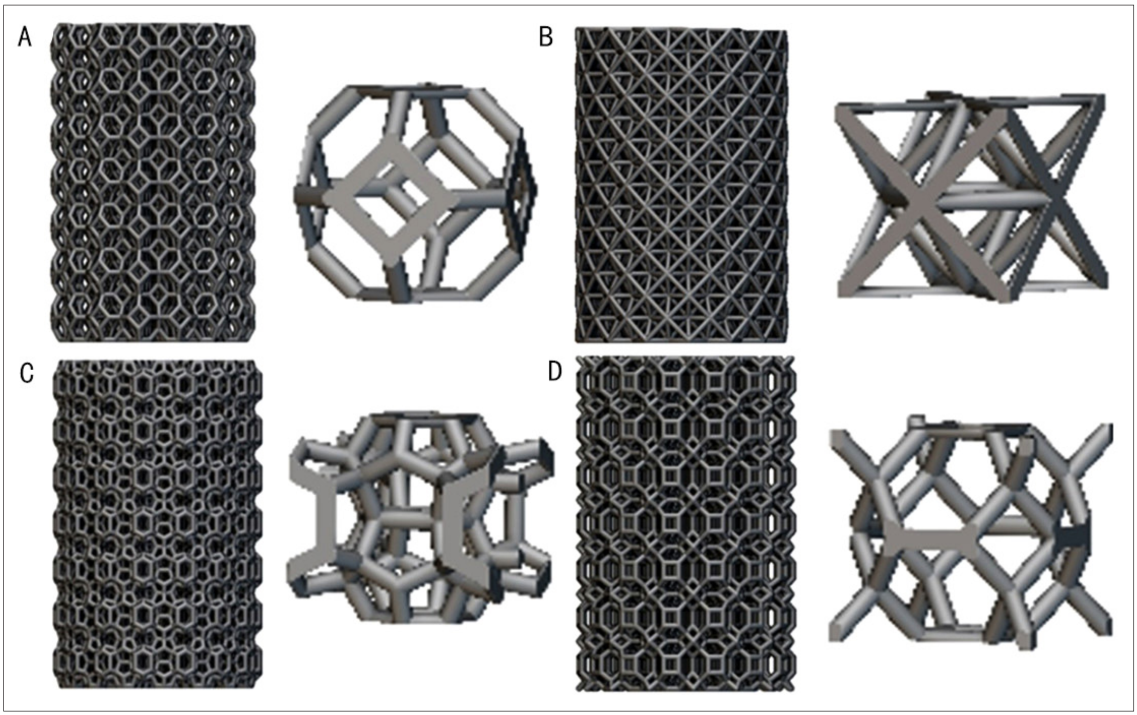

Figure 1. Design of multi-level porous structures with different geometries: (A) Kelvin cell; (B) Octet; (C) Weaire–Phelan; (D) Truncated octahedron.

Table 1. Structural parameters of different porous structures

Porous structure type	Porosity (%)	Average pore size (mm)	Surface area to volume ratio
Octet	74.08	0.28	4.75
Kelvin cell	83.89	0.39	3.28
Weaire–Phelan	68.16	0.25	5.46
Truncated octahedron	78.57	0.33	3.95

0.7 mm, unit height = 1.3 mm, strut diameter = 0.16 mm, roughness peak = 0.07 mm, roughness frequency = 8000, and the number of seeds = 100. The design outcomes are shown in Figure 2.

Table 2 lists the structural parameters of the textured porous structures. Comparison revealed that surface roughness, simplex noise deboss, and Voronoi deboss structures, where surface roughness involved material removal, had slightly higher porosity. In contrast, the Voronoi Emboss structure, where material was added, had slightly lower porosity. Comparing the Kelvin cell structures in Tables 1 and 2, it was found that the porosity increased with material removal and decreased with material addition. The surface-to-volume ratios of surface roughness, simplex noise deboss, and Voronoi emboss structures increased substantially, while the morphology of the Voronoi deboss structure remained largely unchanged. An increase in surface-to-volume ratio may improve biocompatibility to a certain extent.

2.1.3 Kelvin cell structures subjected to Voronoi emboss texturization with different roughness peaks

To investigate the effects of different roughness peaks on biocompatibility, we texturized the Kelvin cell structure using the same parameters outlined in **Section 2.1.2**, but with roughness peaks set at 0.06 mm and 0.08 mm, respectively. The results are presented in Figure 3. Based on the relevant parameters in Table 3, it was found that as the roughness peak increased, both porosity and average pore size decreased, while the surface-to-volume ratio increased.

2.2. Materials and manufacturing methods

The porous structures were fabricated using Ti6Al4V alloy metal powder supplied by Zhejiang Yatong Advanced Materials Co., Ltd., China. The powder composition met the requirements of ASTM F136 and GB/T 13810-2007, as detailed in Table 4. The powder was prepared via gas atomization and had a spherical morphology, with an apparent density (ρ_s) of 2.43 g/cm^3 and a flowability of 36.3 s/50 g. The particle size distribution was narrow, with D90=57.99 μm and D50=35.67 μm.

The molding process was carried out using GYD150 SLM equipment from Shenzhen Sunshine Laser & Electronics Technology Co., Ltd., China. Argon was used as the protective gas, with oxygen content controlled below 0.03%. The process parameters were as follows: laser power = 180W, scanning speed = 500 mm/s, scanning interval = 80 μm, layer thickness = 25 μm, scanning strategy = X–Y interlayer alternating scanning. At least three samples were fabricated for each group.

2.3. Bone defect repair in the distal femur of rabbits via scaffold implantation

To assess the biocompatibility of the porous structures, an *in vivo* animal experiment was carried out at the Veterinary Laboratory of the Animal Health Surveillance Office in Shangzhou district, Shangluo city, Shaanxi province, China. The study was approved by the relevant Ethics Committee. A total of 24 3-month-old rabbits (weighing about 2.5–3.0 kg) were used for the implantation experiment.

Prior to implantation, the materials were first cleaned using an ultrasonic cleaner (Hangzhou BOKE Ultrasonic Equipment Co., Ltd., China), followed by sterilization in an autoclave (160°C for 40 min; Hangzhou Corfied Experimental Instrument Co., Ltd., China). After general anesthesia was administered using xylazine hydrochloride (0.1 mL/kg), a cylindrical bone defect (∅ 5×8 mm) was drilled into the distal femur of each rabbit using an electric drill. A scaffold was randomly implanted into each defect area, and the incision was sutured. The surgical procedure is illustrated in Figure 4. Postoperatively, the rabbits received penicillin for 3 days and were housed individually. After 4 weeks of implantation, the rabbits were euthanized via intravenous injection of an overdose of 3% pentobarbital sodium. The femoral condyles containing the scaffolds were fixed in 10% formalin for subsequent evaluation. 2D cross-sectional images were obtained using a Micro-CT SKYSCAN 1276 scanner (Bruker, Germany).

2.4. Analysis methods

The flow field distribution of blood through different multi-level porous structures was analyzed using Autodesk Simulation CFD 2021 software (Autodesk Software, Inc., United States of America). Animal experiments

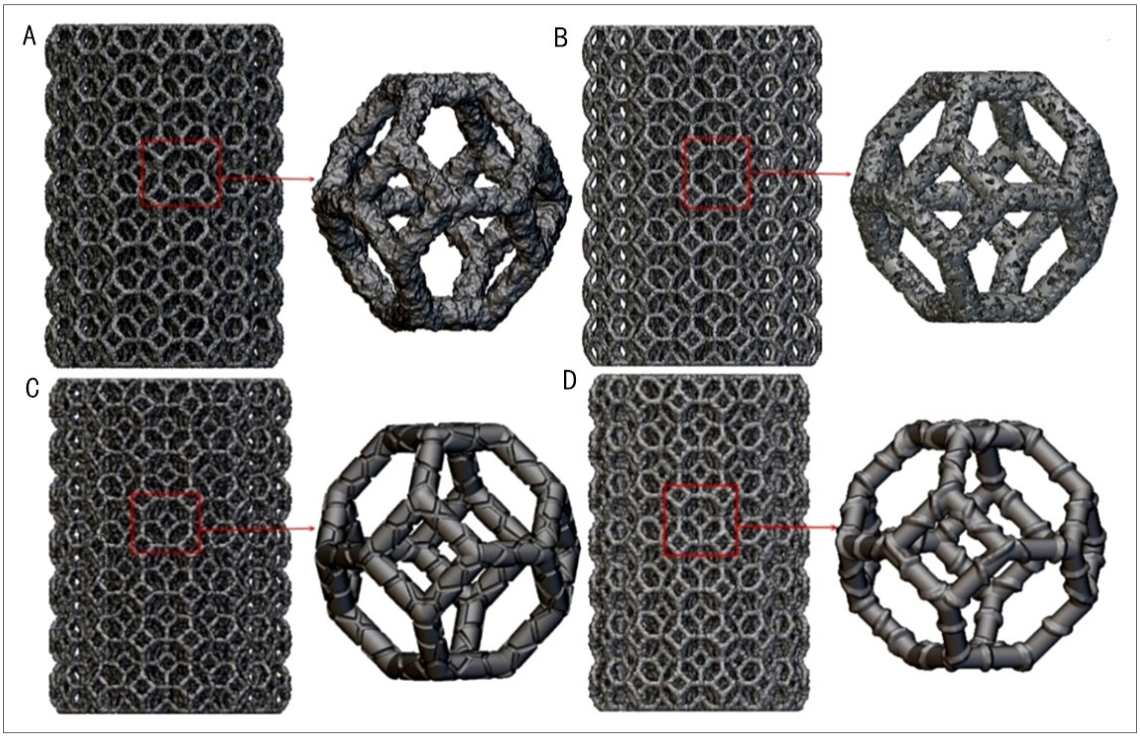

Figure 2. Surfaces of porous structures with different texturizations: (A) Surface roughness; (B) Simplex noise deboss; (C) Voronoi deboss; (D) Voronoi emboss.

Table 2. Structural parameters of different texturizations applied to the Kelvin cell porous structures

Porous structure type	Porosity (%)	Average pore size (mm)	Surface area to volume ratio
Surface roughness	86.89	0.39	3.43
Simplex noise deboss	84.13	0.36	3.66
Voronoi deboss	88.27	0.40	3.29
Voronoi emboss	80.68	0.34	3.59

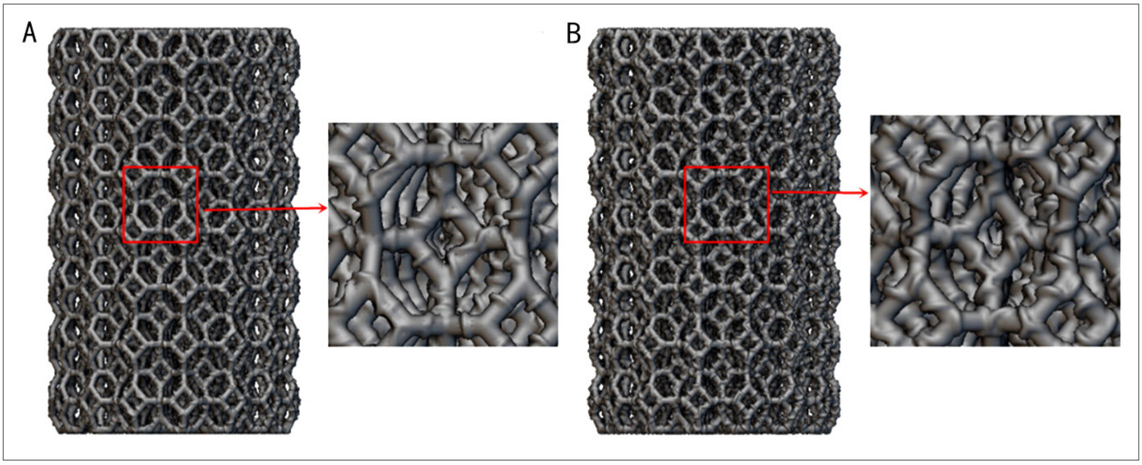

Figure 3. Voronoi emboss textured Kelvin cell structures with different roughness peaks: (A) 0.06 mm; (B) 0.08 mm.

Table 3. Parameters of Kelvin cell structures with Voronoi emboss texturization at different roughness peaks

Porous structure type	Porosity (%)	Average pore size (mm)	Surface area to volume ratio
Voronoi deboss (0.06 mm)	81.72	0.35	3.54
Voronoi deboss (0.08mm)	79.50	0.32	3.70

Table 4. Comparison of powder material manufactured via selective laser melting and the American Society for Testing and Materials (ASTM F136) standard

Element	ti6al4v powder	ASTM f75 standard
Al	5.5–6.75%	5.5–6.5%
V	3.5–4.5%	3.5–4.5%
Fe	0.3%	<0.3%
C	0.08%	<0.08%
N	0.05%	<0.05%
H	0.015%	<0.012%
O	<0.12%	<0.13%
Ti	Balance	Balance

Abbreviations: Al, aluminum; C, carbon; Fe, ferrum; H, hydrogen; O, oxygen; Ti, titanium; V, vanadium.

were conducted to evaluate the biocompatibility of the various porous structures. Four types of surface texturization were applied to the porous structures via secondary programming in Rhinoceros 6.0 (Robert McNeel & Associates, United States of America). The surface morphology of the 3D-printed bone grating plates was observed with a high-definition VGA electron microscope (BOCHENG, China). The effects of different surface texturization methods on biocompatibility were further evaluated through animal experiments. A micro-computed tomography (Micro-CT) SKYSCAN 1276 scanner (Bruker, Germany) was used to obtain tissue ingrowth data within the porous structures and to observe tissue development. The Micro-CT parameters were: pixel resolution = 4032×4032; animal bed resolution = 8 μm; filter = gold + aluminum. For finite element stress analysis, the porous structures in STL format were converted into implicit models using nTop 4.24 software (nTop Software Inc., United States of America). The analysis settings were: units = mm; material = Ti-6Al-4V; mesh type = triangular; mesh size = 0.1 mm; mesh growth rate = 2; boundary conditions = lower end of porous structure fully fixed, 20 N pressure applied at the top.

3. Results

3.1. Mold flow simulation analysis for the porous structures

The presence of “vortex flow” can both dissipate flow energy and increase resistance to fluid entering the center of the scaffold. Moreover, self-circulating flow near the wall forms a barrier between the high-speed, nutrient-rich fluid and the cells on the material surface, which hinders the exchange of metabolic substances.[23] Therefore, further investigation into the flow field distribution of blood within porous structures is necessary to objectively assess the biocompatibility of different porous structures.

3.1.1. Establishment of fluid model

For simulation purposes, the porous structures were designed in a square shape and reduced to a single-layer model. To generate the fluid medium and prevent fluid loss from the sides, 0.15 mm-thick walls were added to the front,

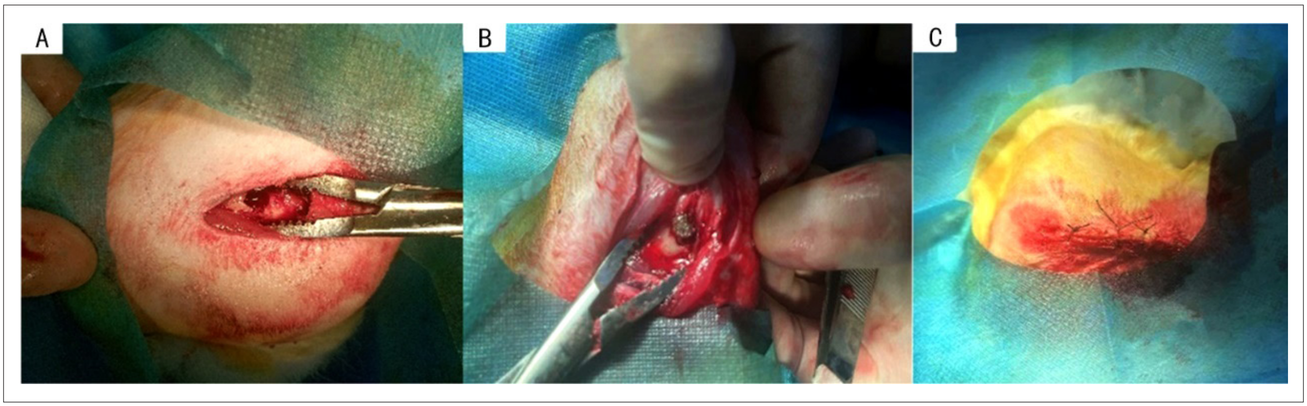

Figure 4. Stent implantation in rabbits: (A) Drilling; (B) Scaffold implantation; (C) Suturing.

back, left, and right of the porous structure to improve the accuracy of the simulation results. The designed porous structure was then split along the centerline with Rhinoceros software to obtain a fluid model cross-section.

The resulting porous structure was imported into Autodesk Simulation CFD software. First, the edges were merged, and then the "Create Surface" command was applied to close the fluid inlet and outlet. The fluid region was generated with the following boundary conditions: "Velocity-inlet" at the inlet, "Pressure-outlet" at the outlet, and "Wall" on all other surfaces, as illustrated in Figure 5. The wall material was defined as TC4, and blood was modeled as an incompressible fluid with a viscosity of 0.033 Pa·s and a density of 1050 kg/m^3. Based on normal human blood flow velocities—125 mm/s for females and 140 mm/s for males—the inlet velocity was set to 140 mm/s, while the outlet pressure was set to 0 Pa. Automatic mesh division was applied.

3.1.2. Flow field analysis

Following the mold flow simulation, the flow field was cut along the direction of blood flow to observe the internal flow distribution, as shown in Figure 6. From Figure 6, it can be observed that when blood entered and exited the octet structure, it encountered a basic unit composed of eight struts. The fluid passed through three of these struts, demonstrating faster flow between them and slower flow at the intersections of the eight struts. This may be due to a vacuum region forming at the strut intersections of the octet structure, making blood entry more difficult.

In contrast, the metamaterial Kelvin Cell structure, featuring a central square formed by four struts, enabled fluid to pass directly through the square, displaying fast central flow that gradually diffused outward. The truncated octahedron and Weaire–Phelan structures, with small squares at the top and bottom and internal pores, allowed fluid to flow through the squares, similarly exhibiting faster central flow and slower peripheral flow. In terms of flow field distribution, the Kelvin Cell structure demonstrated superior characteristics.

The contact area between blood through the porous structure and the strut surfaces is one of the indicators for evaluating biocompatibility. According to the distribution principle of "vortex flow," when liquid encounters an obstacle during motion, it disintegrates and forms a group of mass points rotating around a common axis. Thus, it is necessary to observe the "vortex flow" distribution perpendicular to the blood flow direction. From Figure 7, it can be observed that the octet structure exhibited the strongest vortex intensity, with the center of the vortex located at the strut intersection. The intensity increased outward from the intersection, approaching nearly 0 m/s at the unit's edge. This may be attributed to the closed regions formed at the strut intersections of the octet structure, which are not conducive to blood circulation. In contrast, the Kelvin cell structure demonstrated the weakest vortex intensity, with the vortex spreading outward from the square strut edges and gradually diminishing to nearly 0 m/s at the unit's boundary. The truncated octahedron and Weaire–Phelan structures showed similar vortex distributions, with the vortex flow patterns spreading outward from the small square struts and intensity also diminishing toward the boundaries. In terms of both vortex distribution and intensity, the Kelvin cell structure showed more favorable flow field characteristics.

When fluid flows through the porous structure, higher flow speed and lower pressure are generally more favorable for the exchange of metabolites. Hence, it is important to assess both flow speed and pressure at the inlet of the porous structure to comprehensively evaluate its performance. By measuring the flow speed at the outlet of the porous structure simulation model, we found that the flow speeds were: 139.893 mm/s for the octet structure, 139.824 mm/s for the Kelvin cell, 139.897 mm/s for the truncated octahedron, and 139.769 mm/s for the Weaire–Phelan

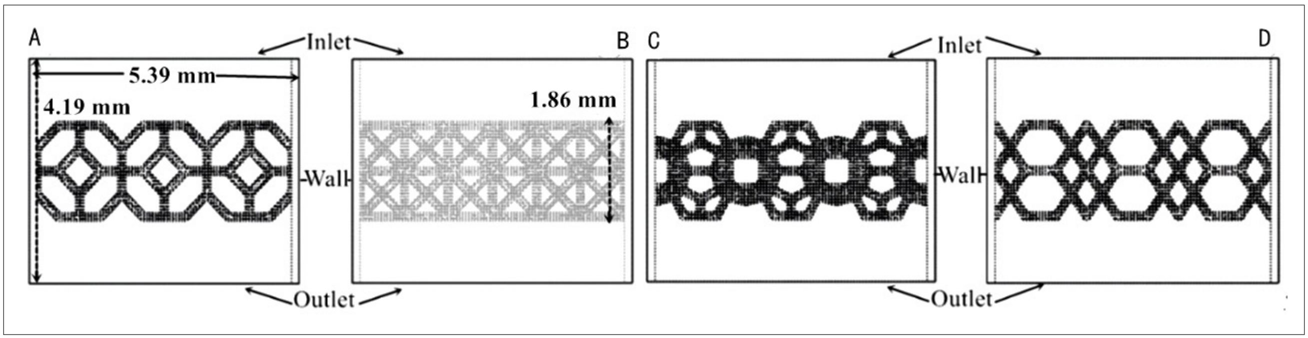

Figure 5. Construction of the fluid model: (A) Kelvin cell; (B) Octet; (C) Truncated octahedron; (D) Weaire–Phelan.

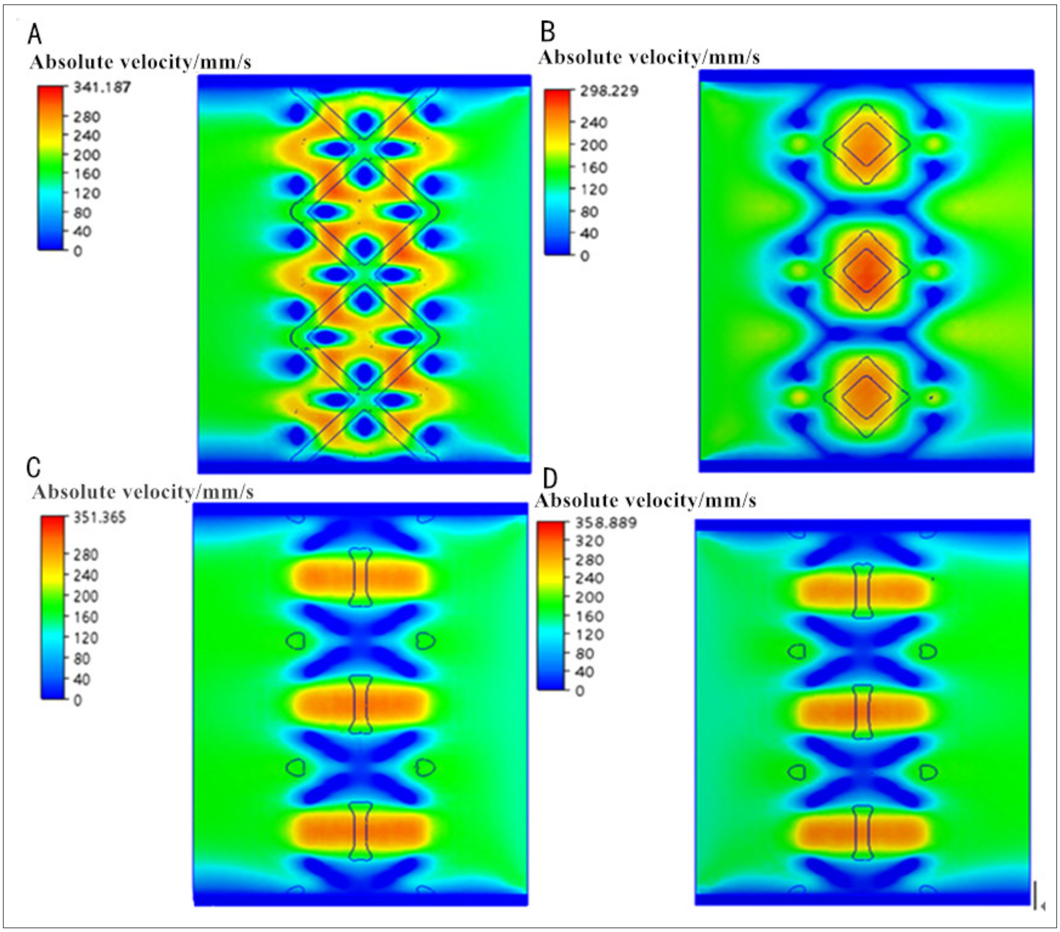

Figure 6. Blood flow analysis of porous structures: (A) Octet; (B) Kelvin cell; (C) Truncated octahedron; (D) Weaire–Phelan.

structure. There was no significant difference between the flow speeds of conventional and metamaterial structures, possibly due to the use of a single-layer structure and the relatively low blood flow speed in the human body. By measuring the pressure at the inlet of the porous structure simulation model, we found: 27,255.1 Pa for octet, 12,241.3 Pa for Kelvin cell, 15,834.9 Pa for truncated octahedron, and 15,977.0 Pa for Weaire–Phelan. Comparison revealed that metamaterial porous structures exhibited lower inlet pressures overall, and the Kelvin cell structure achieved higher flow speeds under lower pressures, demonstrating the best performance among the structures tested.

3.2 Compressive properties simulation analysis of the porous structures

3.2.1. Compression simulation analysis of Kelvin cell porous structures with different texturization methods

Whether the application of surface texturization compromises the mechanical performance of metamaterial porous structures is crucial for the success of implant design. Thus, finite element simulation was used to analyze the fracture behavior of these porous structures and assess their mechanical performance.

Figure 8 shows the finite element analysis results for the textured Kelvin cell structures. From the displacement contour maps (Figures 8A, B, C, and D), it can be observed that under a pressure of 20 N, the displacement of the porous structures was generally small and increased from bottom to top, which is consistent with the typical displacement distribution in loaded components. In descending order, the displacements were: 1.97×10^{-3} mm for Voronoi deboss, 1.38×10^{-3} mm for surface roughness, 1.27×10^{-3} mm for simplex noise deboss, and 9.24×10^{-4} mm for Voronoi emboss. Maximum displacement was inversely proportional to porosity. Texturization methods involving material removal (Voronoi deboss, surface roughness, and simplex noise deboss) resulted in larger displacements, while Voronoi emboss, a material addition method, produced smaller displacements. From the stress contour maps (Figures 8A, B, C, and D), it was observed that stress

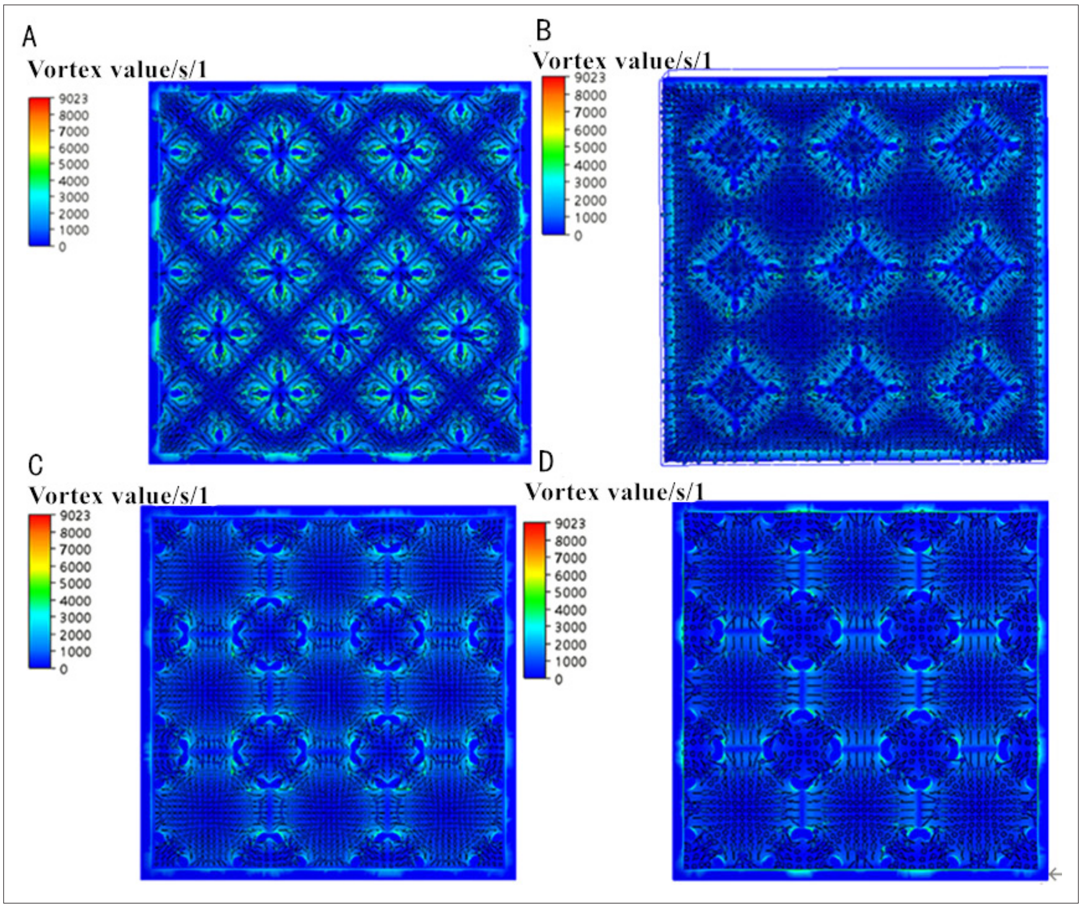

Figure 7. Vortex distribution perpendicular to the blood flow direction in porous structures: (A) Octet; (B) Kelvin cell; (C) Truncated octahedron; (D) Weaire–Phelan.

accumulated along the longitudinal direction in different levels of the porous structures, though the distribution was relatively uniform in both the longitudinal and transverse directions. This may be attributed to the ability of the second-level structure to relieve some of the stress through deformation when subjected to longitudinal pressure. The maximum stress values were: 5.9775×10^3 MPa for simplex noise deboss, 1.05053×10^2 MPa for Voronoi deboss, 1.07689×10^2 MPa for surface roughness, and 8.61795×10^1 MPa for Voronoi emboss. Based on these results, Voronoi Emboss texturization demonstrated better mechanical performance, especially in cases where high porosity is not the primary requirement.

3.2.2. Simulation analysis for Kelvin cell porous structures with Voronoi emboss texturization at different roughness peaks

As previously analyzed, the Kelvin cell structure with Voronoi emboss texturization and a roughness peak of 0.07 mm showed good mechanical performance. To further explore the impact of different roughness peaks on the compressive properties of the Kelvin cell structure, additional simulations were conducted using the parameters described in **Section 2.4**, and the porous structures were analyzed using nTop 4.24 software.

The results are shown in Figure 9. As the roughness peak increased, both stress concentration and displacement of the porous structures under compression decreased. This indicated that the Kelvin Cell structure subjected to Voronoi emboss texturization exhibited improved mechanical performance with a higher roughness peak. However, increasing the roughness peak may lead to reduced porosity and potentially compromise biocompatibility. This trade-off will be further analyzed in future work.

3.3. Analysis of the 3D printing effect of the porous structures

Based on previous findings on the support addition and placement methods for SLM-formed parts,[24] the designed porous structures with varying geometries and subjected to different texturization methods were imported into

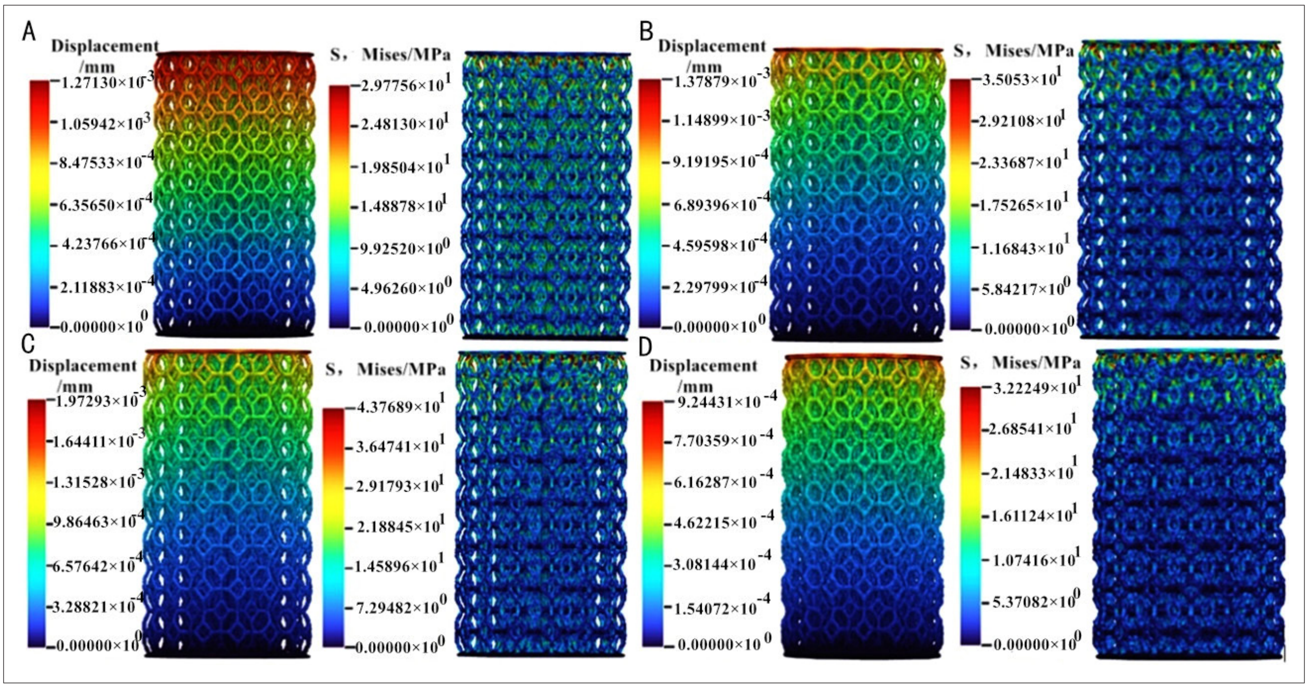

Figure 8. Finite element analysis results for differently textured Kelvin cell porous structures: (A) Simplex noise deboss; (B) Surface roughness; (C) Voronoi deboss; (D) Voronoi emboss.

Materialise Magics 22 software. They were placed vertically in contact with the substrate for slicing, layering, and data processing, and subsequently imported into a metal 3D printer for fabrication.

3.3.1. Analysis of the forming effects of porous structures with different structures

The porous scaffolds printed using the metal 3D printer are shown in Figure 10. Observations of Figure 10 reveal that the porous scaffolds exhibited a bright surface, a clear grid structure, a good metallic texture, minimal slag, and no visible warping or deformation. The intersection between the struts of the porous structure was well-formed, without noticeable collapse visible to the naked eye, indicating that the 3D-printed porous scaffold demonstrated good forming quality and surface integrity. Microscopic examination of the porous structure revealed clear melt tracks and good pore connectivity. Some powder adherence was observed at the pore locations, particularly at the intersection of the struts, though this did not affect subsequent usage.

3.3.2. Analysis of the forming effects of Kelvin cell structures subjected to different texturization methods

Upon examining the 3D-printed texturized porous structure shown in Figure 11, it was found that it had a

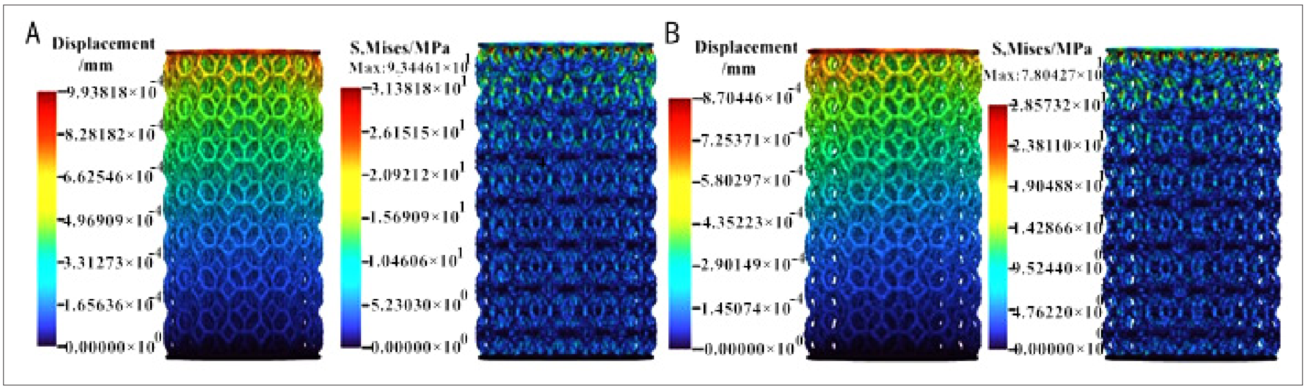

Figure 9. Simulation analysis of Voronoi emboss texturization with different roughness peaks on Kelvin cell porous structures: (A) 0.06 mm; (B) 0.08 mm.

bright surface, clear strut geometry, good metallic texture, no visible warping or deformation, well-formed strut intersections, and no noticeable collapse visible to the naked eye. These observations indicate that the 3D-printed porous structures demonstrated good forming quality and surface finish. Microscopic analysis showed clear melt tracks in the pore structures. However, compared with the surface morphology before texturization, a noticeable increase in slag accumulation and surface roughness was observed after texturization, possibly due to grooves or protrusions introduced by the texturing process. The Voronoi deboss structure, characterized by groove-like surface roughness along the struts, exhibited some strut fractures, although these did not affect its usability. The other texturized porous structures maintained good connectivity.

3.4. Biocompatibility study of the porous structures

3.4.1. Analysis of the repair effect of porous structures with different structures for the bone defects in the distal femur of the rabbits

The scanning data were saved as .bmp format and imported into Mimics Research 20.0 software (Materialise, Belgium) for 3D reconstruction of the porous structures. First, threshold segmentation was conducted using the same threshold values for all four scaffold types (min: −984, max: −929), followed by region growth and 3D reconstruction. As shown in the 3D reconstruction images (Figure 12), bone tissue had grown into the interior of the porous structures within 4 weeks, indicating good biocompatibility of the TC4 material. The Kelvin cell structure exhibited more tissue ingrowth with a denser tissue pattern, with the amount of ingrowth decreasing from the interior to the exterior. This suggests that gradient porosity is beneficial for tissue ingrowth. The slightly reduced ingrowth performance on the exterior of the Kelvin cell structure may be due to its relatively large external pores. With further design optimization, it would be possible to maintain good initial ingrowth while providing sufficient space for continued tissue development. The octet structure exhibited a similar gradient ingrowth pattern, but the internal ingrowth was less dense, possibly due to pore blockage after initial tissue growth. The external pores exhibited good tissue integration, likely due to their smaller pore size. The Weaire–Phelan structure showed complete tissue ingrowth, filling all pores, possibly due to its small pore size. However, excessively small pores of the Weaire–Phelan architecture may hinder material exchange and affect osteogenesis. The truncated octahedron structure demonstrated an ingrowth pattern similar to the Kelvin cell structure, with considerable tissue growth, although the internal ingrowth was slightly less dense, possible due to blockage of smaller pores in the center of the structure. Overall, the Kelvin cell structure exhibited the best tissue ingrowth performance.

3.4.3. Analysis of the repair effect of Kelvin cell structures subjected to different texturization methods on bone defects in the distal femur of rabbits

The data for the Kelvin cell structures with different texturization methods were saved as .bmp format, imported into Mimics Research 20.0 software, and subjected to the same 3D reconstruction process described in **Section 3.4.2**. Observations from Figure 13 revealed that all four types of texturized Kelvin cell structures exhibited good tissue ingrowth. However, compared with the non-

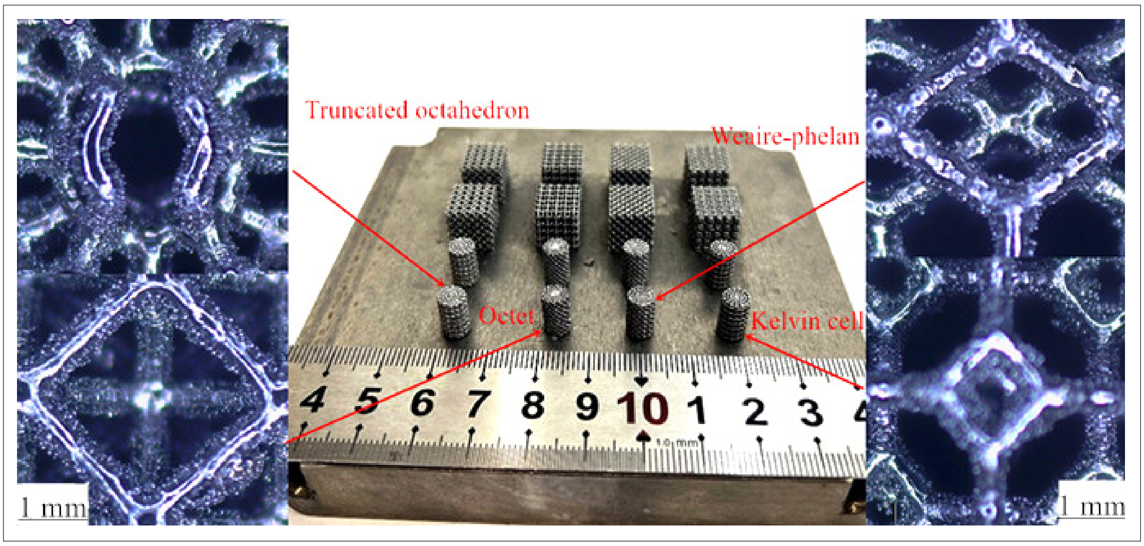

Figure 10. 3D-printed porous structures with different geometries.

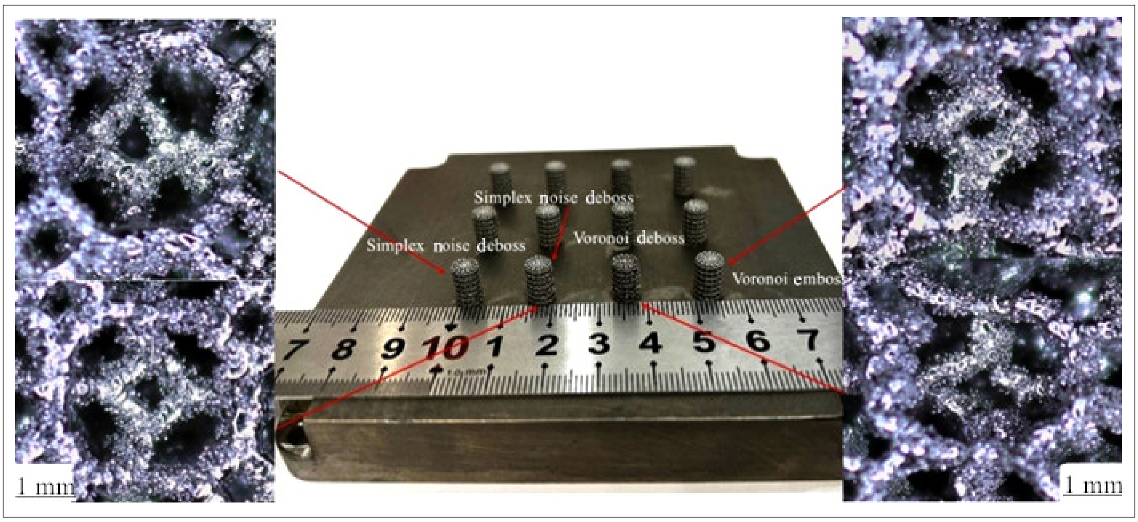

Figure 11. Different texturized porous structures fabricated via 3D printing.

texturized structures, the surface roughness, simplex noise deboss, and Voronoi deboss structures did not significantly promote tissue ingrowth, and in some cases, even showed reduced ingrowth than non-texturized ones. This suggests that increasing surface roughness via material removal slightly increased the surface-to-volume ratio of the porous structure, but was not favorable for tissue integration, thus failing to improve biocompatibility effectively. In contrast, the Voronoi emboss structure showed a gradual decrease in tissue ingrowth from the interior to the exterior. Compared with the non-texturized structures, the Voronoi Emboss structure exhibited significantly improved tissue ingrowth, indicating that increasing surface roughness and surface-to-volume ratio via material addition was more beneficial for tissue ingrowth and could effectively improve biocompatibility. Therefore, in future designs of bio-fixed medical devices, a surface protrusion approach could be considered to enhance the biocompatibility of implants.

3.4.4. Analysis of the repair effect of Kelvin cell structures with Voronoi emboss texturization at different roughness peaks on bone defects in the distal femur of rabbits

By examining Figure 14 and comparing it with Figure 13D, it can be concluded that as the roughness peak increased, bone tissue density at the center of the scaffold also increased. This may be attributed to the gradual decrease in pore size. In terms of tissue adhesion on the scaffold's exterior, a slight increase was observed with increasing roughness peak, possibly resulting from the increased surface-to-volume ratio. Overall, increasing the roughness peak through a convex structure can improve biocompatibility. However, it also reduces pore size, thereby limiting the space available for tissue ingrowth. Therefore, both factors should be considered comprehensively during the actual design process.

4. Discussion

The fluid properties of porous structures directly influence the material exchange efficiency of medical implants. Traditional octet structures, which used eight struts as their basic units, exhibited faster blood flow between three struts and slower flow at the intersections of 8 struts. This fluctuation in local flow speed tends to induce energy loss and is unfavorable for stable material exchange. Metamaterial porous structures perform better in this regard. The Kelvin cell structure demonstrated the characteristic of “fast flow in the center, diffusing to the surrounding area.” The truncated octahedron and Weaire–Phelan structures exhibited a pattern of “fast flow in the center and slow flow in the surrounding area”, which reduced flow speed fluctuations and lowered the overall pressure on the metamaterial, thereby decreasing circulation resistance. The Kelvin cell structure achieved higher flow speed under low pressure and offers the best fluid transmission efficiency, making it an ideal choice for bone implants, tissue scaffolds, and similar applications.

Texturization processes significantly affected the mechanical safety of the Kelvin cell structure. The Voronoi deboss, surface roughness, and simplex noise deboss structures utilized material removal methods, resulting in greater surface displacements. In contrast, the Voronoi emboss structure applied a material addition method, leading to smaller displacements. In terms of stress distribution, the simplex noise deboss structure

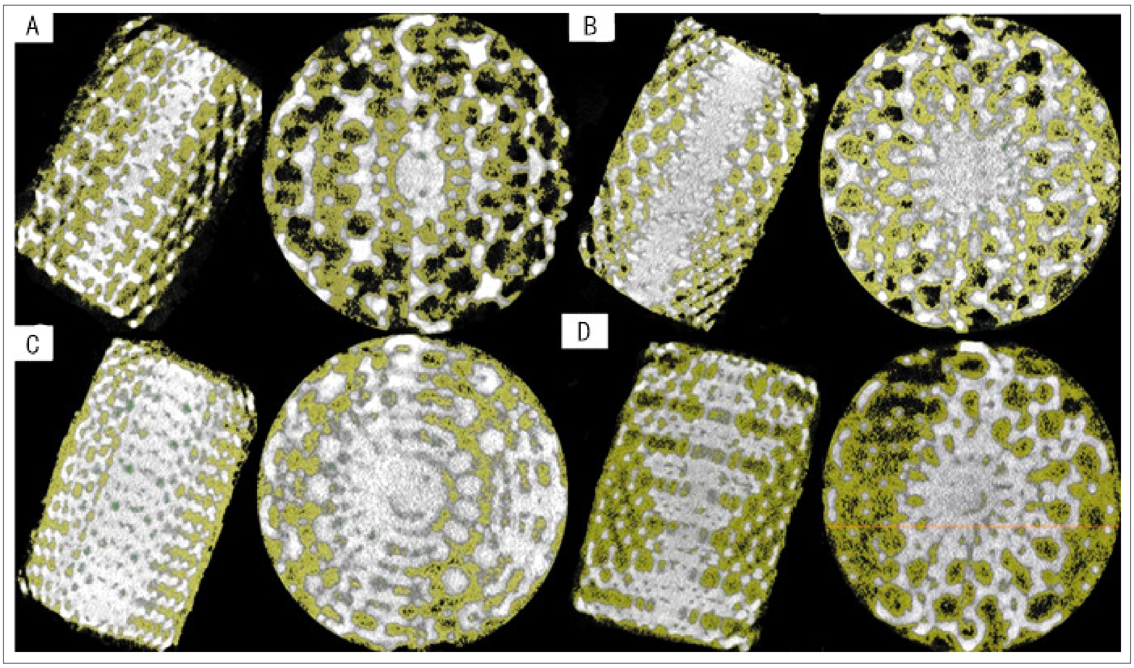

Figure 12. Repair effect of bone defects in the distal femur of rabbits: (A) Kelvin cell; (B) Octet; (C) Weaire–Phelan; (D) Truncated octahedron.

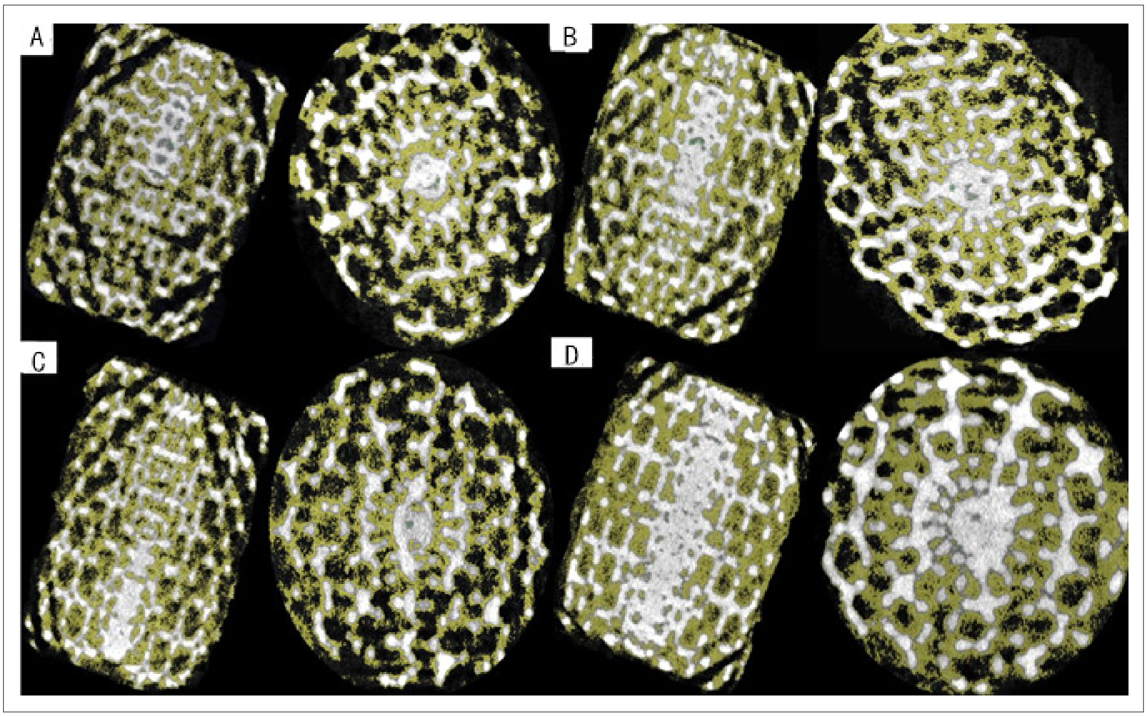

Figure 13. Tissue ingrowth in different textured porous structures: (A) Surface roughness; (B) Simplex noise deboss; (C) Voronoi deboss; (D) Voronoi emboss.

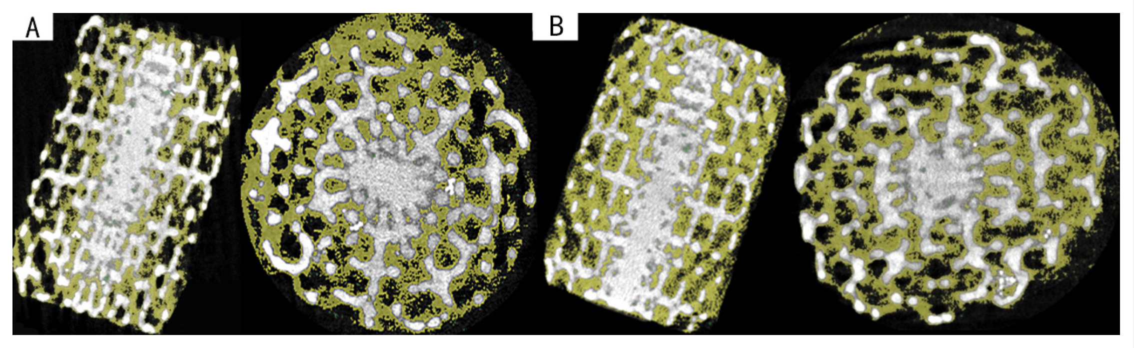

Figure 14. Repair effect of Kelvin cell porous structures with different roughness peaks: (A) 0.06 mm; (B) 0.08 mm.

experienced the highest stress concentration due to its irregular texture, which increases the risk of cracking. The Voronoi deboss and surface roughness structures showed moderate stress concentrations, while the Voronoi emboss structure demonstrated the least stress concentration, with a maximum stress of only 8.61795×10^{1} MPa, meeting mechanical safety requirements. Therefore, in implant design, material addition methods should be prioritized, or material removal parameters should be optimized to minimize structural risks.

The tissue growth effect varied among the different porous structures, with the Kelvin cell structure showing a slightly better performance. These were influenced by factors such as pore gradient, porosity, and potential pore blockage. Texturization introduced a trade-off in biocompatibility. Material removal methods can enhance roughness and increase the surface-to-volume ratio but may compromise pore connectivity, hindering tissue ingrowth. In contrast, material addition methods also enhance roughness but better support tissue integration. Surface protrusions can effectively increase roughness peaks and improve biocompatibility. However, it is important to note that increasing the roughness peak may compress pore space and reduce porosity, thereby limiting deep cellular proliferation. In future work, a quantitative model describing the relationship among roughness, porosity, and tissue ingrowth should be developed to guide collaborative optimization.

5. Conclusion

In the selection of scaffold-type porous structures for medical implants, the Kelvin cell structure demonstrated the best overall performance. It not only achieved high flow velocity and low circulation resistance under low-pressure conditions through its flow field characteristic of "rapid central flow and peripheral diffusion," but also exhibited slightly superior cell growth performance. Therefore, it is an ideal choice for applications such as bone implants and tissue scaffolds. The traditional octahedral structure has limited applicability due to significant local flow velocity fluctuations and high energy loss. Although the truncated octahedron and Weaire–Phelan structures help mitigate flow velocity fluctuations, their fluid transport efficiency remains lower than that of the Kelvin Cell structure.

To ensure the mechanical safety and biocompatibility of Kelvin cell structures, implant design should prioritize material addition processes (such as Voronoi emboss) to reduce the risk of stress concentration and minimize surface displacement. If material removal processes such as Voronoi deboss, surface roughness, or simplex noise deboss are used, parameter optimization (such as controlling removal depth and optimizing texture regularity) is necessary to reduce the risks of cracking and pore connectivity damage, while balancing roughness improvement with structural integrity.

This study presents a preliminary exploration of the fluid characteristics, mechanical safety, and tissue growth effects of porous structures. However, it does not include cell growth experiments, implant site applicability analysis, or histological staining. Future research should include dynamic mechanical testing to evaluate impact resistance, provide biocompatibility direct evidence through cell growth experiments, and clarify the application scope of the structures based on the physiological needs of different implantation sites. Additionally, a quantitative model of "roughness–porosity –tissue growth" should be established to enable multi-parameter collaborative optimization, laying the groundwork for the development of high-performance 3D-printed medical implants.

Acknowledgments

The manufacturing and observation of the femoral prosthesis described in this article were carried out at the Key Laboratory of Special Processing, Zhoukou city.

Funding

The study was funded by the National Natural Science Foundation of China (grant no. 52575470), Natural Science Foundation Project of Henan Province (grant no. 252300421971) and the Zhoukou Science and Technology Plan Project (grant no. ZKSKJGG 100084).

Conflict of interest

The authors declare no conflicts of interest.

Ethics approval and consent to participate

The *in vivo* animal experiment was approved by the Agricultural and Rural Affairs Bureauof Shangzhou District Ethical Review Report (2025922)

Author contributions

Conceptualization: Guoqing Zhang
Formal analysis: Guoqing Zhang, Yongsheng Zhou, Juanjuan Xie
Funding acquisition: Guoqing Zhang
Investigation: Guoqing Zhang, Junxin Li, Congcong Shangguan, Yuchao Bai
Methodology: Guoqing Zhang
Writing–original draft: Guoqing Zhang, Yongsheng Zhou
Writing–review & editing: Guoqing Zhang, Aibing Huang

Consent for publication

Not applicable.

Availability of data

The datasets generated and/or analyzed during the current study are not publicly available due to confidentiality requirements but are available from the corresponding author upon reasonable request.

References

1. Chinese Osteoporosis and Mineral Diseases Society. Guidelines for the diagnosis and treatment of primary osteoporosis (2022). *Chin J Gen Pract*. 2023;26(14):1671-1691. doi: 10.12114/j.issn.1007-9572.2023.0121.
2. Wu Y, Wang Y, Liu M, *et al*. Design, manufacturing, and application of porous implants based on 3D printing technology. *Chin J Med Devices*. 2024;48(01):15-19. doi: CNKI: SUN:ZYLZ.0.2024-01-004.
3. Salaha ZFM, Ammarullah MI, Abdullah NNAA, *et al*. Biomechanical effects of the porous structure of gyroid and voronoi hip implants: a finite element analysis using an experimentally validated model. *Materials*. 2023;16(9):3298. doi: 10.3390/ma16093298
4. Jandyal A, Chaturvedi I, Wazir I, Raina A, Haq MIU. 3D printing–a review of processes, materials and applications in industry 4.0. *Sustain Oper Comput*. 2022;3:33-42. doi: 10.1016/j.susoc.2021.09.004
5. Leschok M, Cheibas I, Piccioni V, *et al*. 3D printing facades: design, fabrication, and assessment methods. *Autom Constr*. 2023;152:104918. doi: 10.1016/j.autcon.2023.104918
6. Li, K, Ji C, Bai S, Jiang B, Pan F. Selective laser melting of magnesium alloys: necessity, formability, performance, optimization and applications. *J Mater Sci Technol*. 2023;154:65-93. doi: 10.1016/j.jmst.2022.12.053
7. Wang H. *Comparative Study on the Application of Personalized Titanium Alloy Prostheses and Allogeneic Mandibular Bones for Mandibular Defect Repair in Beagle Dogs*. Beijing: Chinese People's Liberation Army Medical College; 2017.
8. Yang J, Li Y, Shi X, *et al*. Design and analysis of three-dimensional printing of a porous titanium scaffold. *BMC Musculoskelet Dis*. 2021;22(1):654. doi: 10.1186/s12891-021-04520-1
9. Wang Y. *Experimental Study on Biomechanical Properties and Biocompatibility of 3D Printed Artificial Trabecular Prosthesis*. Zhengzhou University; 2021.
10. Wang S, Gao K, Xu Z, *et al*. 3D printing-assisted traditional steel plate internal fixation for complex tibial plateau fractures. *Chin J Tissue Eng Res*. 2022;26(18):2823-2827. doi: 10.12307/2022.688.
11. Zhang P, Jiang B, Zhang L, *et al*. Biocompatibility evaluation of 3D printed porous tantalum. *Med Equip*. 2022; 35(09):44-49. doi: CNKI: SUN: YLZB.0. 2022-09-014.
12. Liang H, Li R, Liu G, *et al*. Research and clinical application status of porous structure design for medical orthopedic implants. *J Clin Rehabil Tissue Eng Res*. 2017;21(15):2410-2417. doi: CNKI: SUN:XDKF.0.2017-15-023.
13. Liu C, Wang C, Liu H, *et al*. Mechanical properties and biocompatibility of 3D printed Ti6Al4V titanium alloy scaffolds. *Chin J Nonferrous Metal*. 2018; 28(04):758-765. doi: 10.19476/j.ysxb.1004.0609.2018.04.14
14. Lei H, Zhou Z, Liu J, *et al*. Structural optimization of 3D-printed porous titanium implants promotes bone regeneration for enhanced biological fixation. *ACS Appl Mater Interfaces*. 2025;17(12):18059-18073. doi: 10.1021/acsami.4c22401
15. Tamaddon M, Samizadeh S, Wang L, Blunn G, Liu C. Intrinsic osteoinductivity of porous titanium scaffold for bone tissue engineering. *Int J Biomater*. 2017;2017(1):5093063. doi: 10.1155/2017/5093063

16. Zaharin HA, Abdul Rani AM, Azam FI, *et al*. Effect of unit cell type and pore size on porosity and mechanical behavior of additively manufactured Ti6Al4V scaffolds. *Materials*. 2018;11(12):2402.
doi: 10.3390/ma11122402

17. Zadpoor AA. Bone tissue regeneration: the role of scaffold geometry. *Biomater Sci*. 2015;3(2):231-245.
doi: 10.1039/c4bm00291a

18. Kumar A, Nune KC, Murr LE, Misra RDK. Biocompatibility and mechanical behaviour of three-dimensional scaffolds for biomedical devices: process–structure–property paradigm. *Int Mater Rev*. 2016;61(1):20-45.
doi: 10.1080/09506608.2015.1128310

19. Tu C. *Study on the Biocompatibility of 3D Printed Porous Composite Scaffolds*. Huazhong University of Science and Technology; 2016.

20. Zhao Y, Li H, Guo Y, *et al*. Preparation and biocompatibility study of mPEG-PDLLA/nHAP/TTCP porous bone scaffolds. *J Armed Police Med Coll (Med Ed)*. 2016;25(12):954-958.
doi: 10.16548/j.2095-3720.2016.12.002.

21. Jodati H, Yılmaz B, Evis Z. A review of bioceramic porous scaffolds for hard tissue applications: effects of structural features. *Ceram Int*. 2020;46(10):15725-15739.
doi: 10.1016/j.ceramint.2020.03.192

22. Zheng H. *Research on the Surface Topological Structure Regulation of Degradable Polymer Microspheres and its Effects on Cell Adhesion and Function*. Zhejiang University; 2018.

23. Lai Y. *Basic Research on the Application of Micro-groove Topography and Nano-antibacterial Coating to the Surface of Gingival-crossing Part of Dental Implants*. Fujian Medical University; 2014.

24. Zhang G, Yang Y, Zhang Z, *et al*. Optimization design of support structure for laser selective melting forming parts. *China Laser*. 2016;43(12):59-66.
doi: 10.3788/CJL201643.1202002